Article

Parametric Study on Thermo-Hydraulic Performance of NACA Airfoil Fin PCHEs Channels

Wei Wang [1,*], Liang Ding [1], Fangming Han [2], Yong Shuai [1], Bingxi Li [1] and Bengt Sunden [3,*]

[1] School of Energy Science and Engineering, Harbin Institute of Technology, Harbin 150001, China; leslieding@stu.hit.edu.cn (L.D.); shuaiyong@hit.edu.cn (Y.S.); libx@hit.edu.cn (B.L.)
[2] Aerospace Haiying (Harbin) Titanium Co., Ltd., Harbin 150001, China; hanfangming1@live.cn
[3] Department of Energy Sciences, Lund University, SE 22100 Lund, Sweden
[*] Correspondence: wangwei36@hit.edu.cn (W.W.); bengt.sunden@energy.lth.se (B.S.)

Abstract: In this work, a discontinuous airfoil fin printed circuit heat exchanger (PCHE) was used as a recuperator in a micro gas turbine system. The effects of the airfoil fin geometry parameters (arc height, maximum arc height position, and airfoil thickness) and the airfoil fin arrangements (horizontal and vertical spacings) on the PCHE channel's thermo-hydraulic performance were extensively examined by a numerical parametric study. The flow features, local heat transfer coefficient, and wall shear stress were examined in detail to obtain an enhanced heat transfer mechanism for a better PCHE design. The results show that the heat transfer and flow resistance were mainly increased at the airfoil leading edge owing to a flow jet, whereas the airfoil trailing edge had little effect on the thermo-hydraulic performance. The airfoil thickness was the most significant while the arc height and the vertical spacing were moderately significant to the performance. Moreover, only the airfoil thickness had a significant effect on the PCHE compactness. Based on a comprehensive investigation, two solutions NACA-6230 and -3220 were selected owing to their better thermal performance and smaller pressure drop, respectively, with horizontal spacings of 2 mm and vertical spacings of 2 or 3 mm.

Keywords: printed circuit heat exchanger; NACA airfoil fins; micro gas turbine recuperator; thermo-hydraulic; parametric study

1. Introduction

A printed circuit heat exchanger (PCHE) as a new type of heat exchanger is widely used in high-pressure and high-temperature applications [1]. It possesses a high heat exchange area density (2500 m^2/m^3), high compactness, and a large heat transfer coefficient [2], due to the millimeter-level micro channels. Compared to some special finned surfaces [3,4] and metal foam heat exchangers [5], the unique diffusion welding technology of PCHE can improve its reliability. Because of the above advantages, PCHEs are commonly used in fuel gas supply systems, LNG regasification, and cryogenic applications, supercritical carbon dioxide (sCO_2) systems, and liquefied hydrogen and hydrogen refueling stations.

Apart from the above benefits of PCHE, a key problem of flow resistance needs to be solved when it is used in thermal power cycles. Numerous extensive studies have been conducted on this problem. Four types of PCHE channels have been the most studied [2,6], which are shown in Figure 1. Among these, the straight [7,8] and zigzag [9,10] fins are continuous fin types, whereas the S-type [11] and airfoil fins [12] are discontinuous fin types. Tsuzuki et al. [11] first found that an S-type fin channel has one-fifth the pressure drop of a zigzag channel at an equal heat transfer performance. Kim et al. [12] first designed an airfoil fin PCHE channel using the NACA-0020 model. The simulation results showed that the heat transfer coefficients of the airfoil fin and zigzag channels were similar; however, the pressure drop of the airfoil fin channel was reduced to one-twentieth of that of the zigzag channel.
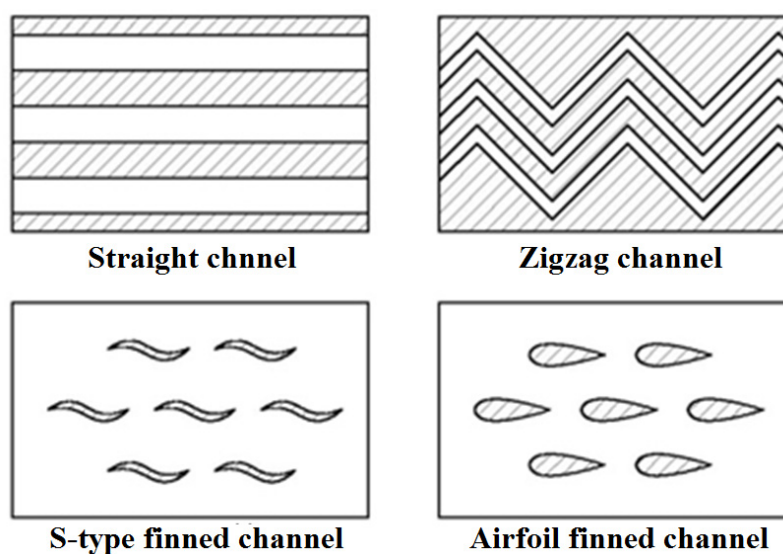
Figure 1. Four kinds of PCHE channels.

Because airfoil fin channels have demonstrated the best thermo-hydraulic performances, many studies have been conducted on airfoil fin PCHE applications in various fields. An experimental study of airfoil fin (NACA-0025) PCHE in a concentrating solar power system was performed by Wang et al. [13], with molten salt as a working fluid. The experimental data presented that the heat transfer performance of the airfoil fin PCHE was superior to the traditional PCHEs with straight and zigzag fins. Chen et al. [14] compared a NACA-00XX airfoil fin PCHE with a conventional zigzag PCHE used in the supercritical carbon dioxide Brayton cycle. The numerical results also presented that the pressure drop of the airfoil fin PCHE was remarkably reduced, and it maintained excellent heat transfer performance. The NACA-0010 airfoil fin PCHE demonstrated better comprehensive performance than the other three PCHEs (0020, 0030, and 0040). Xu et al. [15] performed a numerical study on four discontinuous fin configurations (rectangle, rounded rectangle, ellipse, and airfoil fins) in parallel and staggered arrangements. The results showed that the fin configurations had little effect on the overall thermo-hydraulic performances at low mass flow rates, and the airfoil fin with the staggered arrangement was better than the other types of fins. Chu et al. [16] studied three types of airfoil fin (NACA-8315, 8515, and 8715) PCHEs with consistent and reverse layouts used as condensers in the supercritical CO_2 Brayton power cycle. The results showed that the NACA-8515 airfoil fins with both consistent and reverse layouts on average improved the heat transfer coefficient by 28% and 11% with an increase of the pressure drop by 150% and 22%, respectively, compared with the symmetrical airfoil fins (NACA-0015). Ma et al. [17] employed an airfoil fin PCHE in a very high-temperature reactor and studied the effect of the fin-endwall fillet on the thermo-hydraulic performance. They found that the fin-endwall fillet increased the heat transfer and pressure drop with a longitudinal pitch of 1.63, whereas it had little effect when the longitudinal pitch was above 1.88. Although the above studies have examined airfoil fin PCHEs from different aspects, there is no report on the numerous parameters of airfoil fins and their arrangements. In addition, the enhanced heat transfer mechanism of airfoil fins needs to be clarified to guide PCHE design.

In this work, the discontinuous airfoil fin PCHE was employed as a micro gas turbine recuperator in the extended-range electric vehicle system [18], which has high requirements on heat transfer, pressure drop, and compactness, simultaneously. Therefore, the effects of the airfoil fin parameters (arc height, maximum arc height position, and airfoil thickness) and the airfoil fin arrangements (horizontal and vertical spacings) on the heat transfer and pressure drop were extensively examined by a parametric study. The flow features, local heat transfer coefficient, and wall shear stress were investigated to obtain an enhanced heat transfer mechanism for a better PCHE design.

2. Mathematical Approach

2.1. Physical Model and Boundary Conditions

In this work, the heat transfer and pressure drop of PCHE channels with different NACA airfoil fins were investigated. The structures of the two types of channels are shown in Figure 2. The examined geometrical parameters of the airfoil fin PCHE channels include the horizontal spacing (Lh), vertical spacing (Lv), airfoil chord (Ll), arc height (hl), maximum arc height position (ll), and airfoil thickness (tl), corresponding to the NACA airfoil rules.
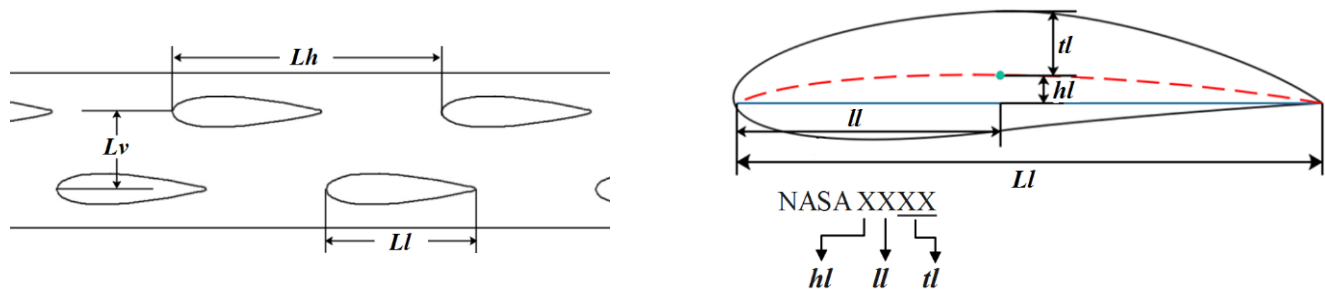

Figure 2. Structure parameters of NACA airfoil fins and arrangements.

The computational domain and boundary conditions are shown in Figure 3. Specifically, the inlet is a velocity boundary with a fixed temperature (T_{in} = 630 K), the outlet is a pressure boundary (P_{out} = 0.3 MPa), the left and right walls are periodic boundaries, and the up, down, and airfoil walls are fixed temperature (T_{wall} = 650 K) walls. The working fluid (compressed air) was incompressible, and its thermo-properties only varied with temperature, as can be seen from Table 1.
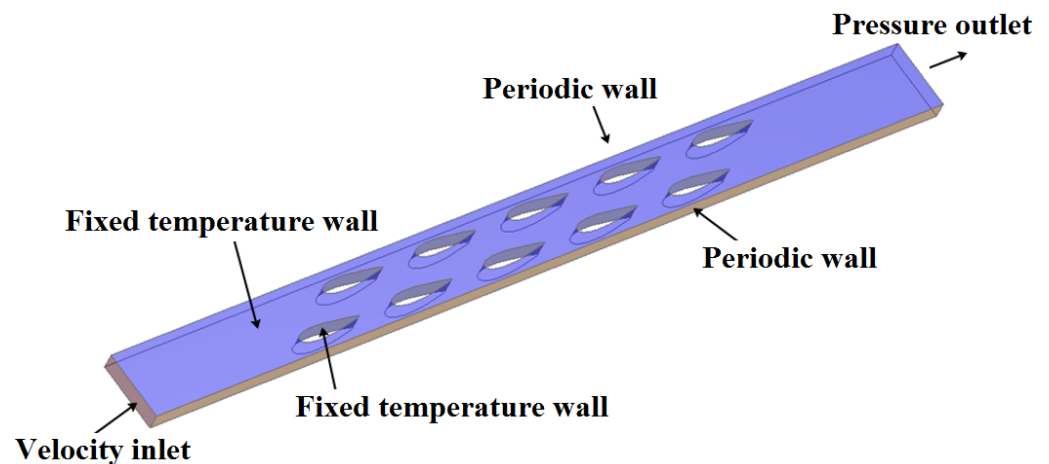

Figure 3. Computational domain and boundary conditions of airfoil fin channels.

Table 1. Thermo-physical properties of cold air (0.3 MPa, 600–720 K) [19].

Equation: $f(T)=c_1 \cdot T^2 + c_2 \cdot T + c_3$				
	ρ (kg/m^3)	C_p (J/kg/K)	λ (W/m/K)	μ (kg/m/s)
c_1	4.801×10^{-6}	4.46×10^{-5}	-1.432×10^{-8}	-1.235×10^{-11}
c_2	-0.009275	0.1777	7.462×10^{-5}	5.021×10^{-8}
c_3	5.969	929.5	0.005678	5.191×10^{-6}

The structured grids were used for the airfoil fin channels' computational domain. The near wall grids were refined with y plus less than 1 [20], as shown in Figure 4. A grid independence test was performed on the NACA-0320 airfoil fin channel, as shown in Figure 5, and the total number of grids was chosen as 892,000.
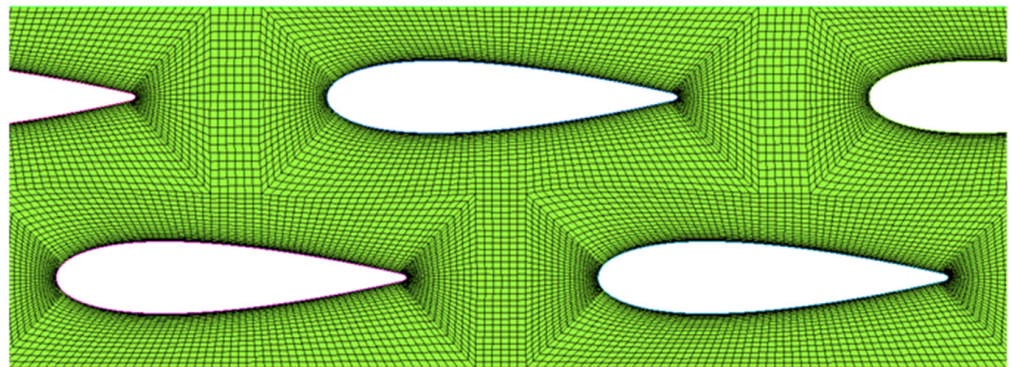
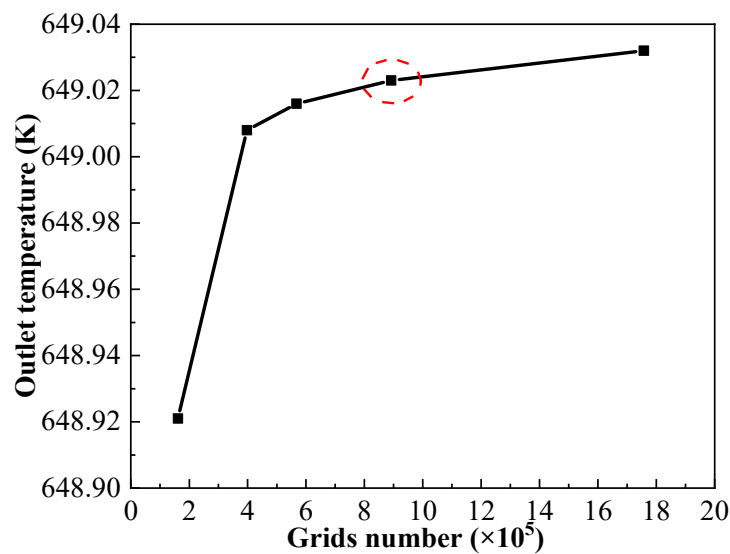**Figure 4.** Computational grids of airfoil fin PCHE channels.

Figure 5. Grid independence test results for the PCHE channel with NACA-0320 airfoil fins.

2.2. Governing Equations and Numerical Approach

In this study, the realizable *k-ε* model was employed [21,22]; the governing equations are given below [23].

The continuity equation is

$$\frac{\partial(\rho u_i)}{\partial x_i} = 0 \tag{1}$$

The momentum equation is

$$\frac{\partial}{\partial x_j}(\rho u_i u_j) = -\frac{\partial P}{\partial x_i} + \frac{\partial}{\partial x_j}[\mu(\frac{\partial u_i}{\partial x_j} + \frac{\partial u_j}{\partial x_i} - \frac{2}{3}\delta_{ij}\frac{\partial u_j}{\partial x_j})] + \frac{\partial}{\partial x_j}(-\rho\overline{u_i'u_j'}) \tag{2}$$

The energy equation is

$$\frac{\partial}{\partial x_i}[u_i(\rho E + P)] = \frac{\partial}{\partial x_i}[(\lambda + \frac{c_P\mu_t}{\mathrm{Pr}_t})\frac{\partial T}{\partial x_j} + \mu u_i(\frac{\partial u_i}{\partial x_j} + \frac{\partial u_j}{\partial x_i} - \frac{2}{3}\delta_{ij}\frac{\partial u_j}{\partial x_j})] \tag{3}$$

where E is the total energy, $E = C_P T - P/\rho + u^2/2$, and λ is the thermal conductivity.

The *k* equation is

$$\frac{\partial}{\partial x_j}(\rho k u_j) = \frac{\partial}{\partial x_j}[(\mu + \frac{\mu_t}{\sigma_k})\frac{\partial k}{\partial x_j}] + G_k - \rho\varepsilon \tag{4}$$

The ε equation is

$$\frac{\partial}{\partial x_j}(\rho \varepsilon u_j) = \frac{\partial}{\partial x_j}[(\mu + \frac{\mu_t}{\sigma_\varepsilon})\frac{\partial \varepsilon}{\partial x_j}] + \rho C_1 S_\varepsilon - \rho C_2 \frac{\varepsilon^2}{k + \sqrt{v\varepsilon}} \tag{5}$$

where G_k represents the production of turbulent kinetic energy and is modeled as $G_k = \mu_t S^2$. The μ_t represents the eddy viscosity and is modeled as $\mu_t = \rho C_\mu k^2 / \varepsilon$ [24].

In the above expressions, $C_1 = \max\left[0.43, \frac{\eta}{\eta+5}\right]$, $S = \sqrt{2S_{ij}S_{ij}}$, $S_{ij} = \frac{1}{2}\left(\frac{\partial u_i}{\partial x_j} + \frac{\partial u_j}{\partial x_i}\right)$, $C_2 = 1.9$, $\sigma_k = 1$, and $\sigma_\varepsilon = 1.2$ [25].

The semi-implicit method for the pressure-linked equations (*SIMPLE*) algorithm was employed on the velocity and pressure equations, and a second-order upwind scheme was employed on the energy and momentum equations. The scaled residuals for all solutions must be less than 10^{-6} [26,27] to obtain convergence.

2.3. Data Reduction

The average convective heat transfer coefficient (h), average pressure drop (ΔP_L), and total average heat flux (Q_A) were employed to assess the heat transfer, flow resistance, and compactness of the PCHEs, respectively [28–30].

$$h = \frac{q}{T_{wall} - 0.5(T_{in} + T_{out})} \tag{6}$$

$$\Delta P_L = \Delta P / L \tag{7}$$

$$Q_A = Q / A \tag{8}$$

where q is the average heat flux, L is the channel length, ΔP is the pressure drop between the inlet and outlet, and A is the area of heat exchange.

2.4. Numerical Model Validation

An experimental work by Ishizuka et al. [31] was used to validate the numerical model in this work. The experimental PCHE is a typically zigzag-type channel with the following geometrical parameters: hot-side channel pitch pl = 9 mm, angle α = 115°, and radius r = 0.95 mm; cold-side channel pitch pl = 7.24 mm, angle α = 100°, and radius r = 0.9 mm. The fluids for the two sides were both supercritical CO_2. The hot-side working fluid is supercritical CO_2; inlet temperature = 553.05 K, inlet pressure = 2.52 MPa, and mass flow rate = 0.867 g/s. The cold-side working fluid is also supercritical CO_2; inlet temperature = 381.05 K, inlet pressure = 8.28 MPa, and mass flow rate = 0.9456 g/s. The comparison of experimental data and the numerical results are shown in Table 2. The maximum error for the cold side is less than ±5%, and the maximum error for the hot side is less than ±1%, which meet the accuracy requirements.

Table 2. Numerical model validation using experimental data [31].

	Experimental	Numerical	Error
Pressure drop of cold side (Pa)	73,220	76,832.0	−3612 (−4.9%)
Pressure drop of hot side (Pa)	24,180	24,381.6	−2016.6 (−0.83%)
Temperature difference of cold side (K)	140.38	146.8	−6.42 (−4.6%)
Temperature difference of hot side (K)	169.6	171.3	−1.7 (−1.0%)

3. Results and Discussion

3.1. Effect of Arc Height (hl)

Four different arc heights (0330, 3330, 6330, and 9330) are compared in Figure 6. With the increase in arc height, the airfoils present more asymmetry, and the convective heat transfer coefficient (h), pressure drop per unit length (ΔP_L), and heat flux per unit area (Q_A) increase but to different extents. The average h values for 3330, 6330, and 9330 are 2.3%, 6.4%, and 8% higher than that for 0330, respectively. In addition, the average ΔP_L values for 3330, 6330, and 9330 are 3.3%, 15.4%, and 27.7% higher than that for 0330, respectively. The above trends suggest that the pressure drop increases rapidly with the increase in hl, whereas the heat transfer performance increase is moderate. Moreover, the Q_A increases slightly with increasing arc height (hl); this means that the hl is dis-significant to the PCHE compactness design.
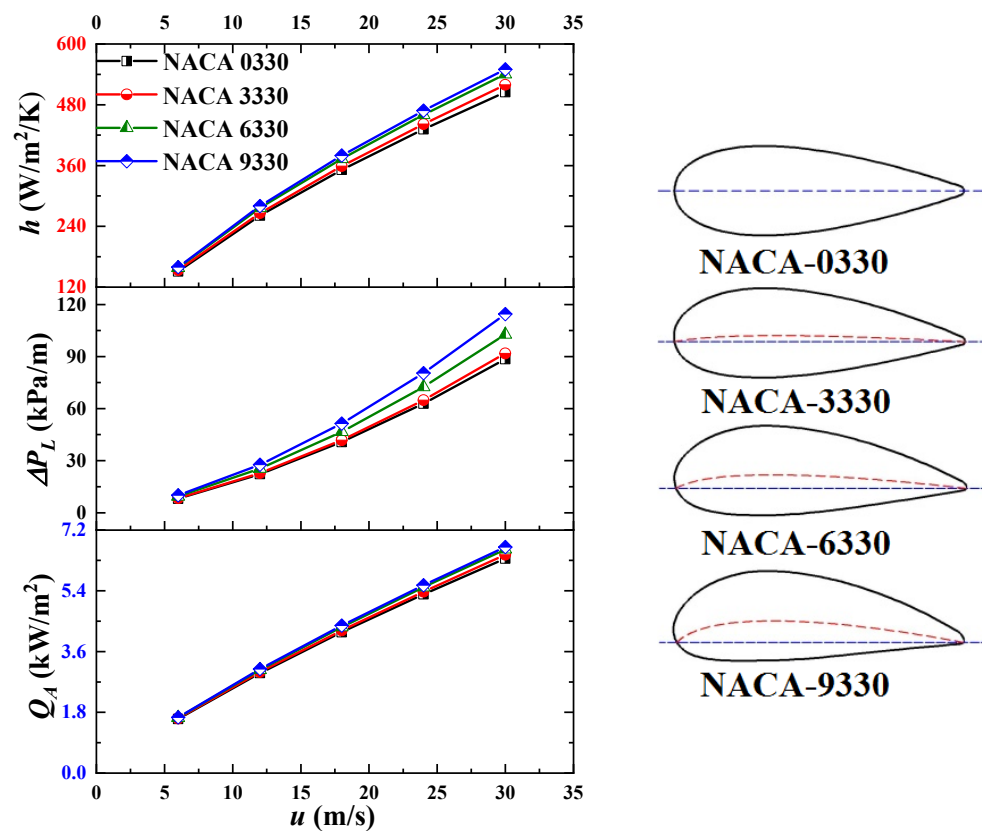

Figure 6. Average performance for different airfoil arc heights (hl).

The distributions of the velocity u, turbulent kinetic energy (TKE), local convective heat transfer coefficient (h_{local}), and wall shear stress (WSS) for NACA-0330 and 9330 are shown in Figure 7. From Figure 7a, velocity u for NACA-0330 is accelerated significantly in the main flow region, whereas for NACA-9330, this occurs near the airfoil surface, which is more beneficial for heat transfer improvement. The TKE for NACA-0330 is remarkable at the airfoil trailing edge, which indicates severe turbulent pulsations (see Figure 7b). The TKE for NACA-9330 is inhibited by the vertical velocity component. Figure 7c shows that the h_{local} reaching the maximum at the airfoil leading edge is due to the jet flow heat transfer being significant (than the convective heat transfer). The h_{local} reach to the minimum at the airfoil trailing edge is due to the secondary flow velocity being very low, causing a thick boundary layer. Moreover, the h_{local} for NACA-0330 in the main flow region and at the airfoil trailing edge is higher than that for NACA-9330, whereas the h_{local} for NACA-9330 in the near-wall region is significantly higher than that for NACA-0330. In Figure 7d, the WSS reflects the flow resistance created by the airfoil fins. It can be seen that the WSS is significant owing to the turbulent flow impingement on the airfoil leading edge, whereas it

is minimum at the airfoil trailing edge owing to a secondary vortex generation. In addition, the WSS for NACA-9330 is overall greater than that for NACA-0330, based on the more drastic impact effect and the lower secondary flow generation of the former.
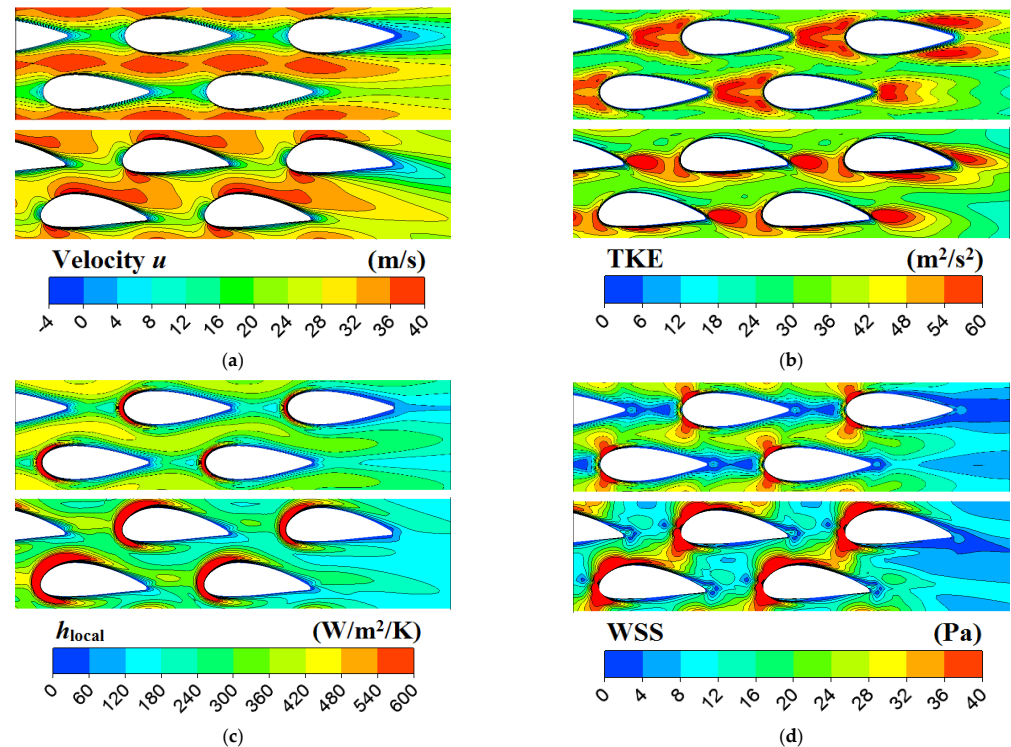

Figure 7. Contours of velocity u, TKE, h_{local}, and WSS for NACA-0330 and -9330 airfoils. (**a**) Velocity u distributions for NACA 0330 and 9330 (middle surface, u_{in} = 18 m/s). (**b**) TKE distributions for NACA 0330 and 9330 (middle surface, u_{in} = 18 m/s). (**c**) h_{local} distributions for NACA 0330 and 9330 (wall surface, u_{in} = 18 m/s). (**d**) WSS distributions for NACA 0330 and 9330 (wall surface, u_{in} = 18 m/s).

3.2. Effect of Maximum Arc Height Position (ll)

The maximum arc height position (*ll*) mainly affects the second half of the airfoil structure, whereas it has a minor effect on the first half, as in the cases of NACA-6220, 6420, 6620, and 6820 shown in Figure 8. The average h, ΔP_L, and Q_A values for the four kinds of *ll* indicate that the *ll* is not significant to the three evaluation performances. Relatively, h and ΔP_L for *ll* < 5 (NACA-6220 and -6420) cause slightly greater effects than that for *ll* > 5 (NACA-6620 and -6820). Moreover, the Q_A values for the four cases are similar.

The distribution of the velocity u, TKE, h_{local}, and WSS for NACA-6220 and -6820 are shown in Figure 9. The velocity u for NACA-6220 presents a high acceleration at the airfoil leading edge, whereas it exhibits a low back flow at the airfoil trailing edge. The TKE for NACA-6820 is significantly higher than that for NACA-6220 after the airfoil trailing edge. The above flow feature causes the h_{local} for NACA-6220 to be much higher at the airfoil leading edge than that for NACA-6280. In comparison, the h_{local} for NACA-6820 is much higher in the main flow region than that for NACA-6220 owing to the high TKE distribution. The WSSs also present similar tendencies as the h_{local} distributions for NACA-6220 and -6820, which are also determined by the flow features. In comparison, the partial differences between the h_{local} and the WSS do not cause remarkable variations in the overall performance, as shown in Figure 8.
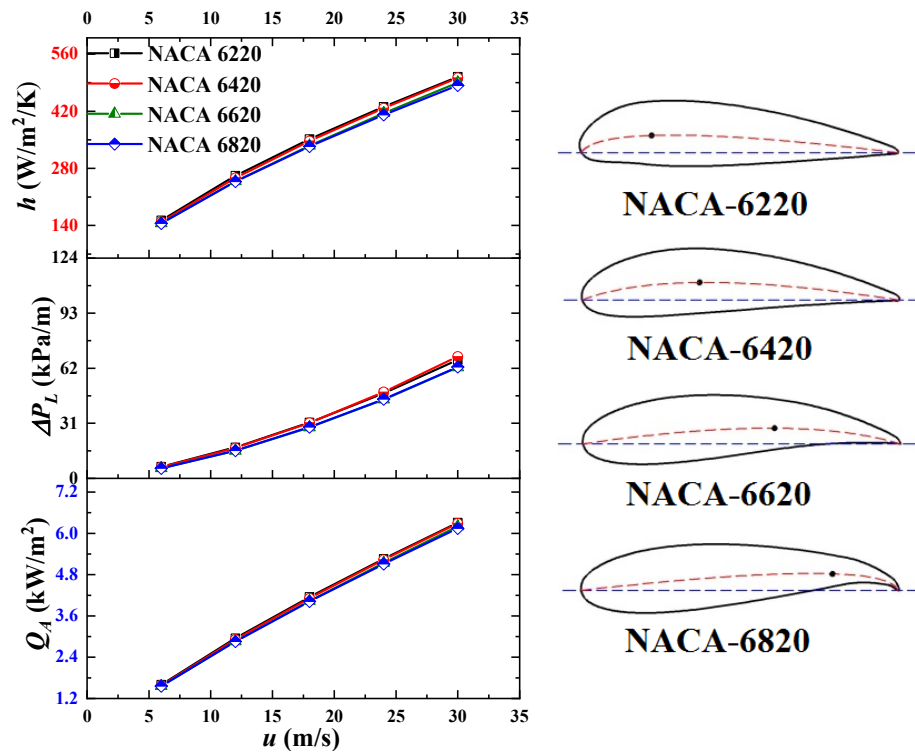
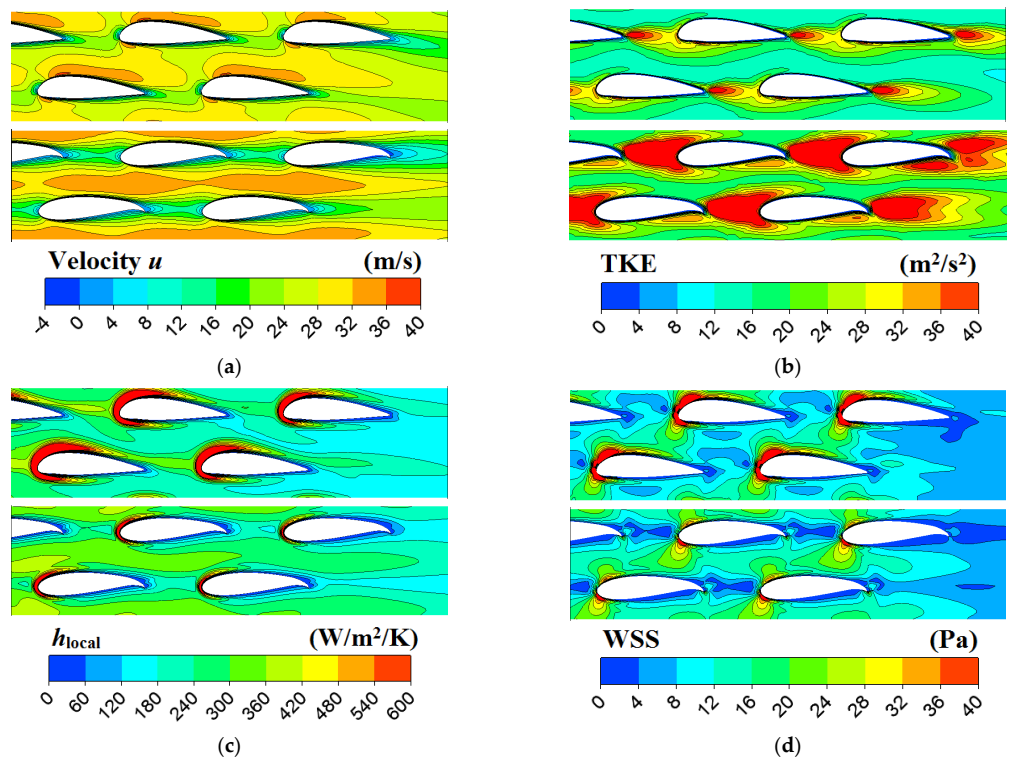**Figure 8.** Average performances for different locations of maximum arc height (*ll*).

Figure 9. Contours of velocity *u*, TKE, h_{local}, and WSS for NACA-6220 and 6820 airfoils. (**a**) Velocity *u* distributions for NACA 6220 and 6820 (middle surface, u_{in} = 18 m/s). (**b**) TKE distributions for NACA 6220 and 6820 (middle surface, u_{in} = 18 m/s). (**c**) h_{local} distributions for NACA 6220 and 6820 (wall surface, u_{in} = 18 m/s). (**d**) WSS distributions for NACA 6220 and 6820 (wall surface, u_{in} = 18 m/s).

3.3. Effect of Airfoil Thickness (tl)

The effect of the airfoil thickness (tl) on the average performance is shown in Figure 10. The structure diagrams show significant differences among the four cases. The width increases with the increase in tl, and the average h, ΔP_L, and Q_A are all obviously heightened with the increase in tl. The average h for 0320, 0330, and 0340 are 9.58%, 21.4%, and 33.8% higher than that of 0310, respectively. The average ΔP_L for 0320, 0330, and 0340 are 38.1%, 113%, and 246.25% higher than that of 0310, respectively. Additionally, the increase in airfoil thickness is an advantage to improve the PCHE compactness.

The distributions of the velocity u, TKE, h_{local}, and WSS for NACA-0310 and 0340 are shown in Figure 11. The velocity u for NACA-0310 shows a relatively uniform distribution, owing to the small distribution of the narrow airfoil. In comparison, the velocity u for NACA-0340 presents a severe acceleration between two rows of the airfoils, owing to the reduction in the cross-section area by the large width of the airfoils. In addition, the velocity u distribution shown in the red dotted frame in Figure 11a indicates that although the large tl causes a high-intensity reverse flow at the airfoil trailing edge, it is inhibited by the accelerating fluid. NACA-0340 has an extremely higher TKE than NACA-0310 and, partially, the TKE can be up to 10 times higher. The h_{local} and WSS for NACA-0340 present significant increases at the airfoil leading edge because the increase in the windward area causes a remarkable jet flow effect. In comparison, the h_{local} and NACA-WSS for 0340 are slightly increased by the interstitial flows.
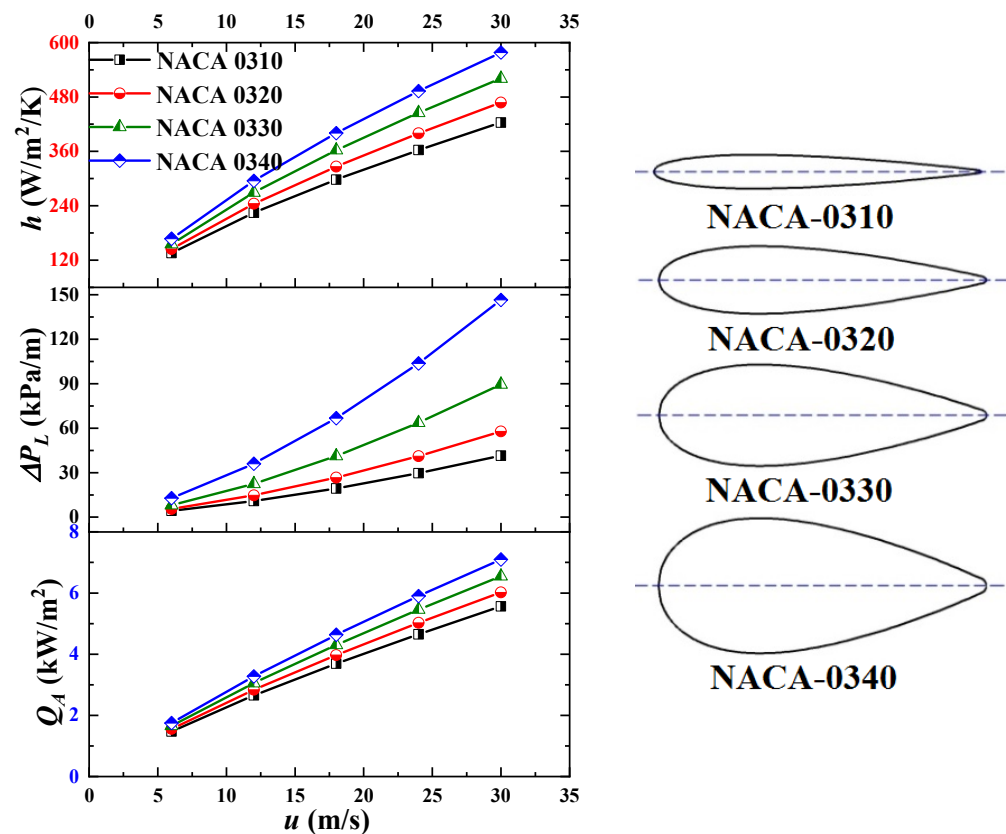

Figure 10. Average performance for different airfoil thicknesses (tl).

3.4. Effects of Horizontal Spacing (Lh) and Vertical Spacing (Lv)

The average performance for different horizontal spacing (Lh) is shown in Figure 12. The h, ΔP_L, and Q_A slightly decrease with the increase in Lh. The average h values of $Lh = 3$, 4, and 5 mm are 2.2%, 4.1%, and 6.4% lower than that of $Lh = 2$ mm, respectively. The average ΔP_L of $Lh = 3$, 4, and 5 mm are 6.2%, 9.6%, and 12.2% lower than that of $Lh = 2$ mm, respectively. From Figure 13, it can be seen that the h_{local} and WSS distributions for two cases ($Lh = 2$ and 5 mm) are similar around the airfoil walls. This suggests that the variation

in *Lh* has no effect on the enhanced heat transfer mechanism, and the variation rate of the average performance is uniform. This is because of the secondary flow at each airfoil trailing edge, which leads to a periodic flow redevelopment.

The average performance for different vertical spacings (*Lv*) is shown in Figure 14. The average *h* of *Lv* = 3, 4, and 5 mm are 4.2%, 6.4%, and 6.6% lower than that of *Lv* = 2 mm. The average ΔP_L of *Lv* = 3, 4, and 5 mm are 26.3%, 37.1%, and 42% lower than that of *Lv* = 2 mm, respectively. The average *h* and ΔP_L show that the performances of *Lv* = 4, and 5 mm are quite propinquity. It means that when *Lv* is above 3 mm, the vortices caused by the airfoils are not coupled to each other anymore. Moreover, the *Lv* > 3 mm is not suggested due to the compactness demands. From a comprehensive point, the *Lv* = 3 mm is suggested due to the average *h* being smaller—lower than that of *Lv* = 2 mm, and the average ΔP_L is significantly lower than that of *Lv* = 2 mm. The global distributions of the velocity *u*, TKE, h_{local}, and WSS for *Lv* = 2 mm in Figure 15, also show that the disturbed flow and turbulent pulsation between the two rows of the airfoils are superimposed, fundamentally causing the heat transfer and flow resistance to increase. In comparison, the corresponding distribution for *Lv* = 5 mm suggests that the complex flow features caused by the airfoils are independent of each other.
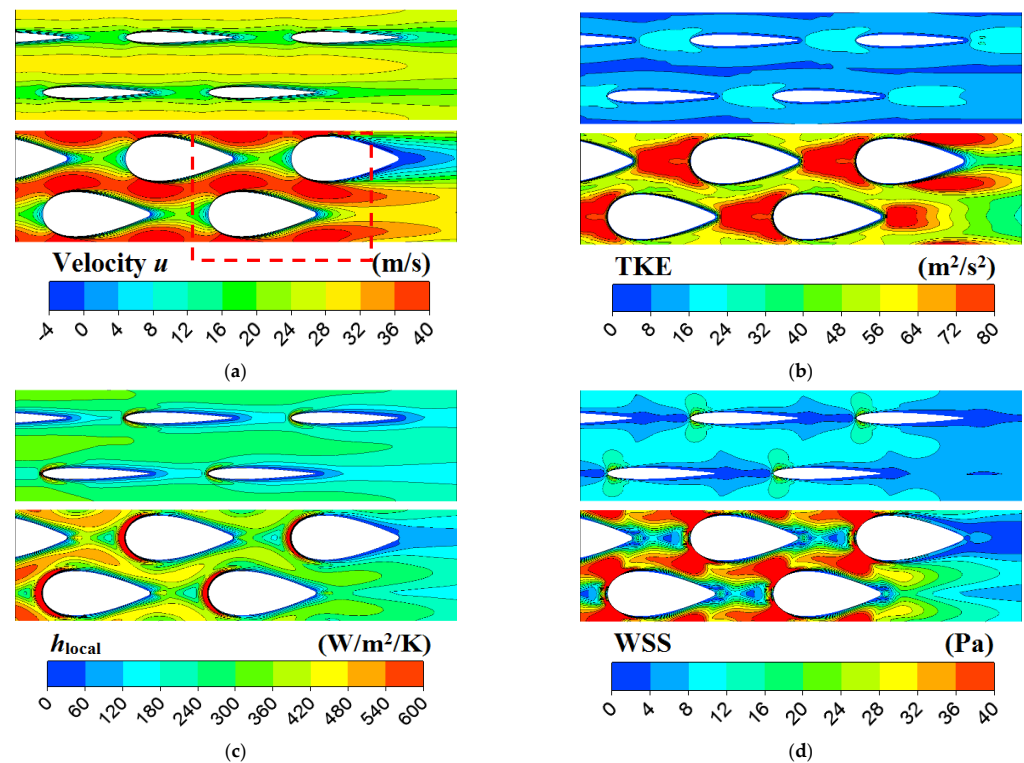

Figure 11. Contours of velocity *u*, TKE, h_{local}, and WSS for NACA-0310 and 0340 airfoils. (**a**) Velocity *u* distributions for NACA 0310 and 0340 (middle surface, u_{in} = 18 m/s). (**b**) TKE distributions for NACA 0310 and 0340 (middle surface, u_{in} = 18 m/s). (**c**) h_{local} distributions for NACA 0310 and 0340 (wall surface, u_{in} = 18 m/s). (**d**) WSS distributions for NACA 0310 and 0340 (wall surface, u_{in} = 18 m/s).
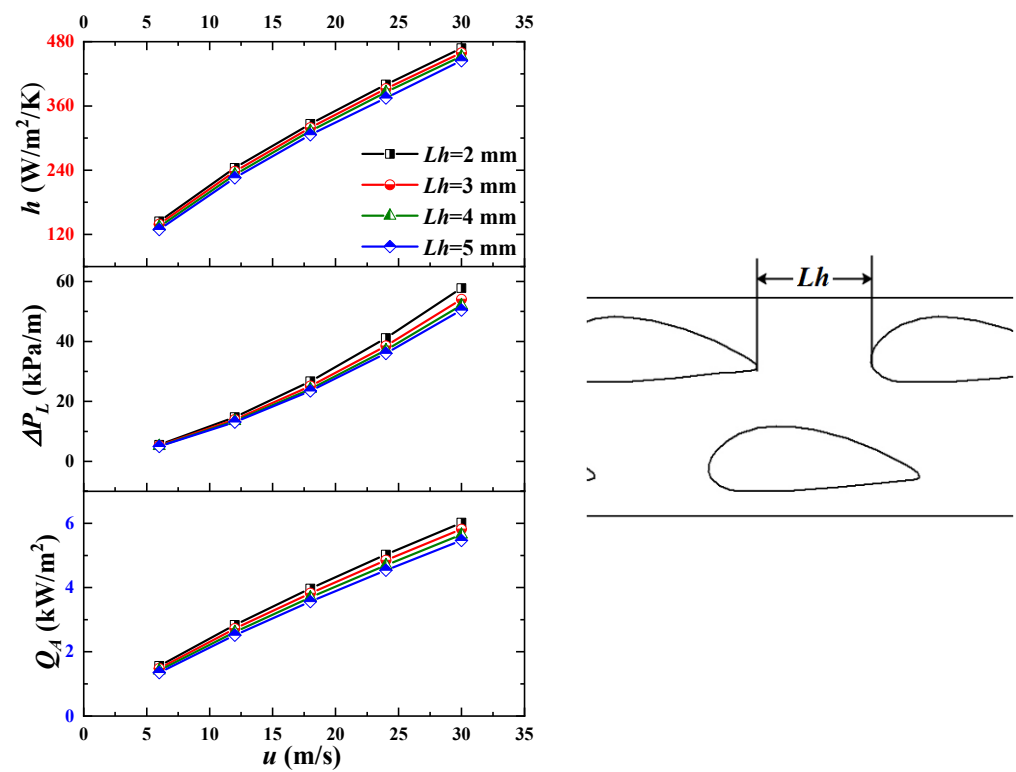
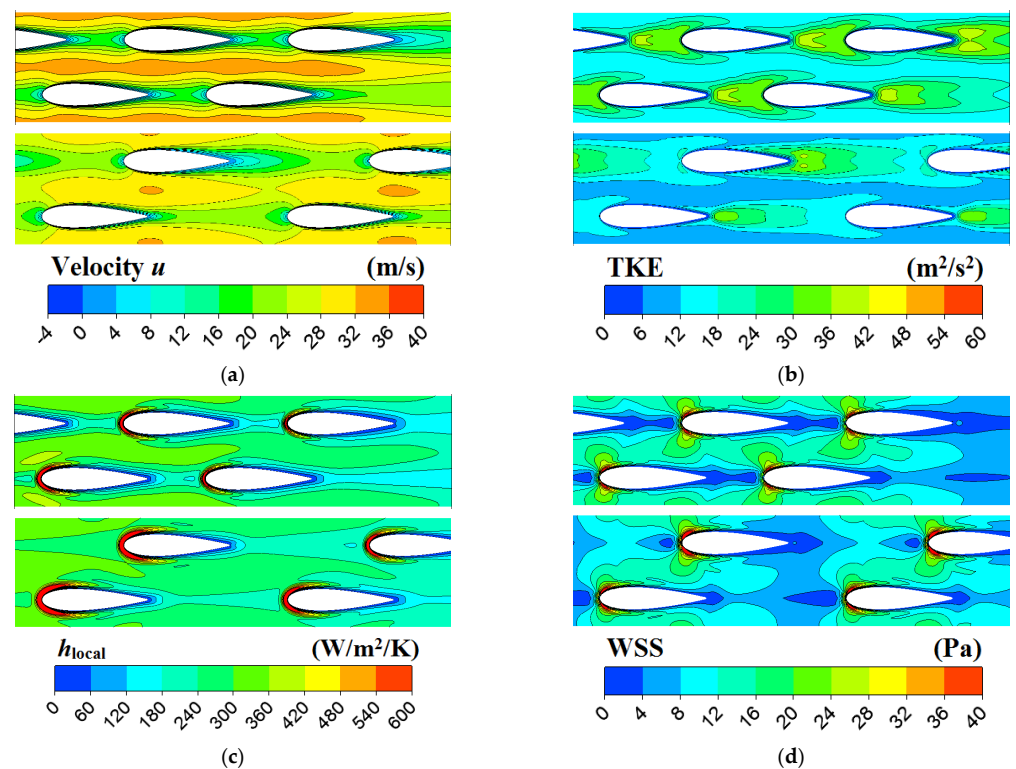**Figure 12.** Average performance for different horizontal spacings (*Lh*).

Figure 13. Contours of velocity *u*, TKE, h_{local}, and WSS for *Lh* = 2 and 5 mm with NACA-0320. (**a**) Velocity *u* distributions for *Lh* = 2 and 5 mm (0320, middle surface, u_{in} = 18 m/s). (**b**) TKE distributions for *Lh* = 2 and 5 mm (0320, middle surface, u_{in} = 18 m/s). (**c**) h_{local} distributions for *Lh* = 2 and 5 mm (0320, wall surface, u_{in} = 18 m/s). (**d**) WSS distributions for *Lh* = 2 and 5 mm (0320, wall surface, u_{in} = 18 m/s).
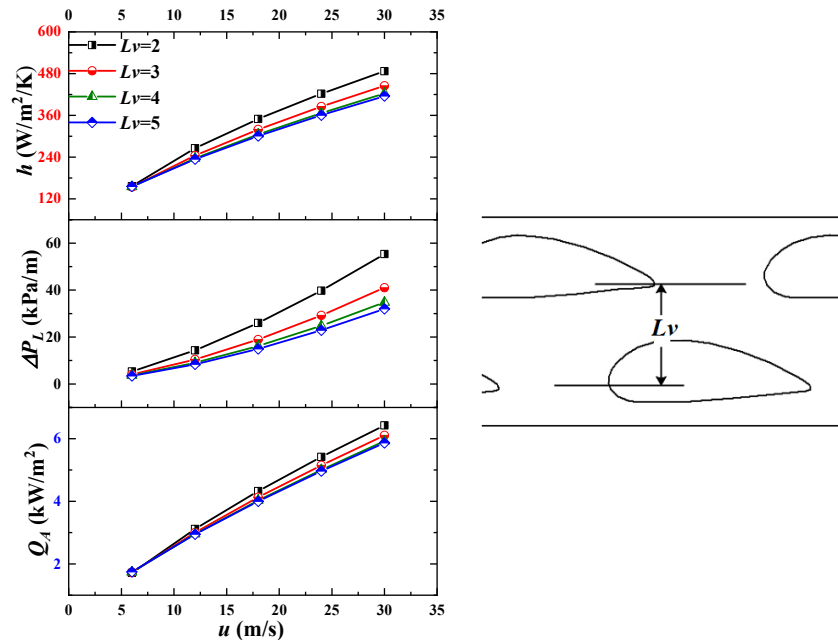
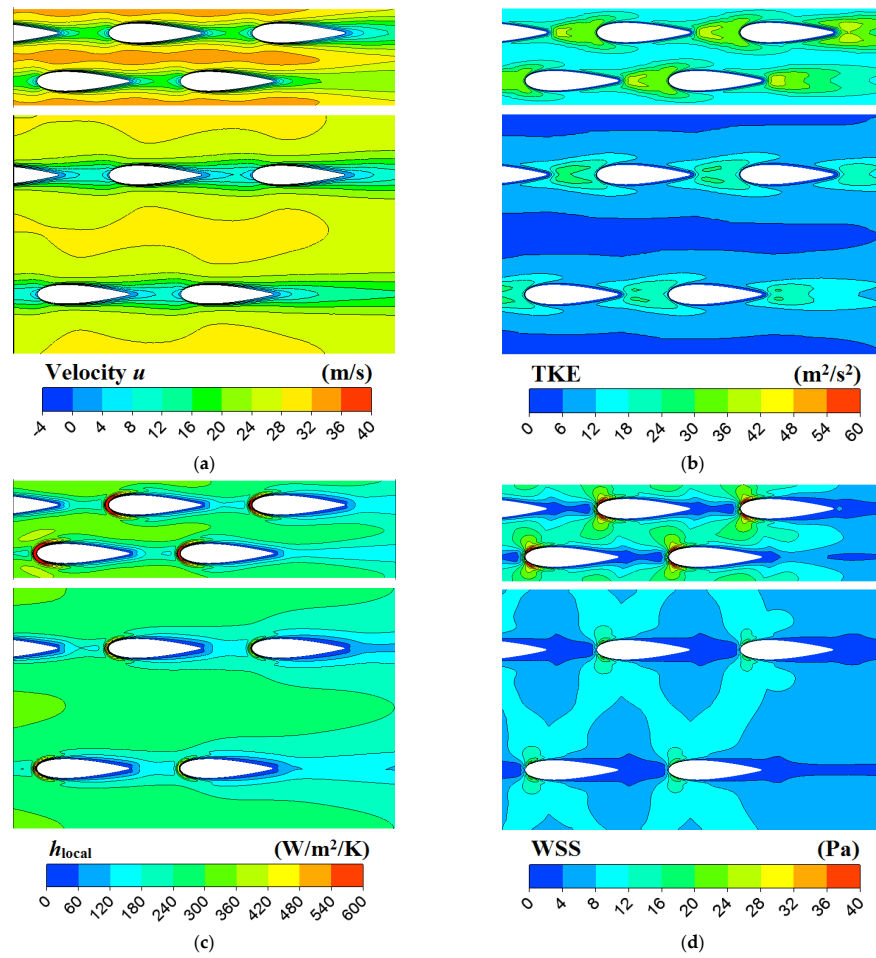**Figure 14.** Average performance for different vertical spacings (*Lv*).

Figure 15. Contours of velocity *u*, TKE, h_{local}, and WSS for *Lv* = 2 and 5 mm with NACA-0320. (**a**) Velocity *u* distributions for *Lv* = 2 and 5 mm (0320, middle surface, u_{in} = 18 m/s). (**b**) TKE distributions for *Lv* = 2 and 5 mm (0320, middle surface, u_{in} = 18 m/s). (**c**) h_{local} distributions for *Lv* = 2 and 5 mm (0320, wall surface, u_{in} = 18 m/s). (**d**) WSS distributions for *Lv* = 2 and 5 mm (0320, wall surface, u_{in} = 18 m/s).

4. Conclusions

In this study, airfoil fins PCHEs were employed as micro gas turbine recuperators for extended-range electric vehicles, and the thermo-hydraulic performances of PCHE channels with airfoil fins were numerically studied. Five geometric parameters, i.e., arc height (*hl*), maximum arc height position (*ll*), airfoil thickness (*tl*) horizontal spacing (*Lh*), and vertical spacing (*Lv*) were examined in detail, and the enhanced heat transfer mechanism was analyzed. The main conclusions are summarized as follows:

(1) The heat transfer and the flow resistance are mainly increased at the airfoil leading edge owing to the flow jet. A secondary vortex is produced at the airfoil trailing edge, causing a violent turbulent pulsation; however, it has a minor effect on the heat transfer improvement.

(2) Among the five geometrical parameters, the airfoil thickness (*tl*) is the most significant. The arc height (*hl*) and the vertical spacing (*Lv*) are moderately significant, whereas the maximum arc height position (*ll*) and the horizontal spacing (*Lh*) are almost insignificant to the thermo-hydraulic performance. Moreover, only the airfoil thickness has a significant effect on the PCHE compactness.

(3) Two solutions (NACA-6230 and -3220) were selected for their better thermal performance and smaller pressure drop, respectively, with *Lh* = 2 mm and *Lv* = 2 or 3 mm.

Nomenclature

A	Area (m^2)
C_1, C_2	Realizable k-ε model constants
Cp	Specific heat (J/kg/K)
E	Internal energy (J/kg)
h	Heat transfer coefficient ($W/m^2/K$)
L	Length (m)
Lh, *Lv*	Horizontal and vertical spacing (mm)
Ll, *hl*, *ll*, *tl*	Airfoil chord, arc height, maximum are height position and airfoil thickness
T	Temperature (K)
TKE	Turbulent kinetic energy (J/kg)
P	Pressure (Pa)
PCHE	Printed circuit heat exchanger
Pr	Prandtl number
Q	Heat flux (W)
u, *v*, *w*	Streamwise, transverse, and vertical velocity components (m/s)
WSS	Wall shear stress

Greek letters	
ε	Turbulence dissipation rate (m^3/s^2)
λ	Thermal conductivity (W/m/K)
μ	Dynamic viscosity (kg/m/s)
ρ	Density of fluid (kg/m^3)
Subscripts	
in, out	Inlet and outlet
i, j, k	Directions of the coordinate system
wall	Wall

References

1. Chen, M.; Sun, X.; Christensen, R.N.; Shi, S.; Skavdahl, I.; Utgikar, V.; Sabharwall, P. Experimental and numerical study of a printed circuit heat exchanger. *Ann. Nucl. Energy* **2016**, *97*, 221–231. [CrossRef]
2. Huang, C.; Cai, W.; Wang, Y.; Liu, Y.; Li, Q.; Li, B. Review on the characteristics of flow and heat transfer in printed circuit heat exchangers. *Appl. Therm. Eng.* **2019**, *153*, 190–205. [CrossRef]
3. Batista, J.; Trp, A.; Lenic, K. Heat Transfer Enhancement of Crossflow Air-to-Water Fin-and-Tube Heat Exchanger by Using Delta-Winglet Type Vortex Generators. *Energies* **2022**, *15*, 2070. [CrossRef]
4. Altwieb, M.; Mishra, R.; Aliyu, A.M.; Kubiak, K.J. Heat Transfer Enhancement by Perforated and Louvred Fin Heat Exchangers. *Energies* **2022**, *15*, 400. [CrossRef]
5. Hmad, A.A.; Dukhan, N. Cooling Design for PEM Fuel-Cell Stacks Employing Air and Metal Foam: Simulation and Experiment. *Energies* **2021**, *14*, 2687. [CrossRef]
6. Yoon, S.H.; No, H.C.; Kang, G.B. Assessment of straight, zigzag, S-shape, and airfoil PCHEs for intermediate heat exchangers of HTGRs and SFRs. *Nucl. Eng. Des.* **2014**, *270*, 334–343. [CrossRef]
7. Chu, W.-X.; Li, X.-H.; Ma, T.; Chen, Y.-T.; Wang, Q.-W. Experimental investigation on SCO2-water heat transfer characteristics in a printed circuit heat exchanger with straight channels. *Int. J. Heat Mass Transf.* **2017**, *113*, 184–194. [CrossRef]
8. Jiang, Y.; Liese, E.; Zitney, S.E.; Bhattacharyya, D. Design and dynamic modeling of printed circuit heat exchangers for supercritical carbon dioxide Brayton power cycles. *Appl. Energy* **2018**, *231*, 1019–1032. [CrossRef]
9. Kim, J.H.; Baek, S.; Jeong, S.; Jung, J. Hydraulic performance of a microchannel PCHE. *Appl. Therm. Eng.* **2010**, *30*, 2157–2162. [CrossRef]
10. Meshram, A.; Jaiswal, A.K.; Khivsara, S.D.; Ortega, J.D.; Ho, C.; Bapat, R.; Dutta, P. Modeling and analysis of a printed circuit heat exchanger for supercritical CO2 power cycle applications. *Appl. Therm. Eng.* **2016**, *109*, 861–870. [CrossRef]
11. Tsuzuki, N.; Kato, Y.; Ishiduka, T. High performance printed circuit heat exchanger. *Appl. Therm. Eng.* **2007**, *27*, 1702–1707. [CrossRef]
12. Kim, D.E.; Kim, M.H.; Cha, J.E.; Kim, S.O. Numerical investigation on thermal–hydraulic performance of new printed circuit heat exchanger model. *Nucl. Eng. Des.* **2008**, *238*, 3269–3276. [CrossRef]
13. Wang, W.-Q.; Qiu, Y.; He, Y.-L.; Shi, H.-Y. Experimental study on the heat transfer performance of a molten-salt printed circuit heat exchanger with airfoil fins for concentrating solar power. *Int. J. Heat Mass Transf.* **2019**, *135*, 837–846. [CrossRef]
14. Chen, F.; Zhang, L.; Huai, X.; Li, J.; Zhang, H.; Liu, Z. Comprehensive performance comparison of airfoil fin PCHEs with NACA 00XX series airfoil. *Nucl. Eng. Des.* **2017**, *315*, 42–50. [CrossRef]
15. Xu, X.Y.; Wang, Q.W.; Li, L.; Ekkad, S.V.; Ma, T. Thermal-Hydraulic Performance of Different Discontinuous Fins Used in a Printed Circuit Heat Exchanger for Supercritical CO_2. *Numer. Heat Transf. Part A Appl.* **2015**, *68*, 1067–1086. [CrossRef]
16. Chu, W.-X.; Bennett, K.; Cheng, J.; Chen, Y.-T.; Wang, Q.-W. Thermo-Hydraulic Performance of Printed Circuit Heat Exchanger with Different Cambered Airfoil Fins. *Heat Transf. Eng.* **2019**, *41*, 708–722. [CrossRef]
17. Ma, T.; Xin, F.; Li, L.; Xu, X.-Y.; Chen, Y.-T.; Wang, Q.-W. Effect of fin-endwall fillet on thermal hydraulic performance of airfoil printed circuit heat exchanger. *Appl. Therm. Eng.* **2015**, *89*, 1087–1095. [CrossRef]
18. Xiao, G.; Yang, T.; Liu, H.; Ni, D.; Ferrari, M.L.; Li, M.; Luo, Z.; Cen, K.; Ni, M. Recuperators for micro gas turbines: A review. *Appl. Energy* **2017**, *197*, 83–99. [CrossRef]
19. Wang, W.; Li, B.; Tan, Y.; Li, B.; Shuai, Y. Multi-objective optimal design of NACA airfoil fin PCHE recuperator for micro-gas turbine systems. *Appl. Therm. Eng.* **2021**, *204*, 117864. [CrossRef]
20. Mauro, G.M.; Iasiello, M.; Bianco, N.; Chiu, W.K.S.; Naso, V. Mono- and Multi-Objective CFD Optimization of Graded Foam-Filled Channels. *Materials* **2022**, *15*, 968. [CrossRef]
21. Fernández, I.; Sedano, L. Design analysis of a lead–lithium/supercritical CO2 Printed Circuit Heat Exchanger for primary power recovery. *Fusion Eng. Des.* **2013**, *88*, 2427–2430. [CrossRef]
22. Wang, W.; Shuai, Y.; Li, B.; Li, B.; Lee, K.-S. Enhanced heat transfer performance for multi-tube heat exchangers with various tube arrangements. *Int. J. Heat Mass Transf.* **2021**, *168*, 120905. [CrossRef]
23. Fluent, A. *Ansys Fluent Theory Guide*; ANSYS Inc.: Canonsburg, PN, USA, 2011; Volume 15317, pp. 724–746.
24. Shih, T.-H.; Liou, W.W.; Shabbir, A.; Yang, Z.; Zhu, J. A new k-ε eddy viscosity model for high reynolds number turbulent flows. *Comput. Fluids* **1995**, *24*, 227–238. [CrossRef]

25. Versteeg, W.M.H.K. *An Introduction to Computational Fluid Dynamics: The Finite Volume Method*, 2nd ed.; Prentice Hall: Harlow, UK, 2007.

26. Wang, W.; Zhang, Y.; Li, B.; Han, H.; Gao, X. Influence of geometrical parameters on turbulent flow and heat transfer characteristics in outward helically corrugated tubes. *Energy Convers. Manag.* **2017**, *136*, 294–306. [CrossRef]

27. Feng, Y.-Y.; Wang, C.-H. Discontinuous finite element method applied to transient pure and coupled radiative heat transfer. *Int. Commun. Heat Mass Transf.* **2021**, *122*, 105156. [CrossRef]

28. Wang, W.; Shuai, Y.; Ding, L.; Li, B.; Sundén, B. Investigation of complex flow and heat transfer mechanism in multi-tube heat exchanger with different arrangement corrugated tube. *Int. J. Therm. Sci.* **2021**, *167*, 107010. [CrossRef]

29. NematpourKeshteli, A.; Iasiello, M.; Langella, G.; Bianco, N. Enhancing PCMs thermal conductivity: A comparison among porous metal foams, nanoparticles and finned surfaces in triplex tube heat exchangers. *Appl. Therm. Eng.* **2022**, *212*, 118623. [CrossRef]

30. Sun, K.; Zhou, G.-Y.; Luo, X.; Tu, S.-T.; Huang, Y.-Y. Study on enhanced heat transfer performance of open-cell metal foams based on a hexahedron model. *Numer. Heat Transfer Part A Appl.* **2022**, 1–21. [CrossRef]

31. Ishizuka, T. Thermal-Hydraulic Characteristics of a Printed Circuit Heat Exchanger in a Supercritical CO_2 Loop. In Proceedings of the 11th International Topical Meeting on Nuclear Reactor Thermal-Hydraulics, Avignon, France, 2–6 October 2005.